



The Strong Rotation of M5 (NGC 5904) as Seen from the MIKIS Survey of Galactic Globular Clusters*

B. Lanzoni^{1,2}, F. R. Ferraro^{1,2}, A. Mucciarelli^{1,2}, C. Pallanca^{1,2}, E. Lapenna^{1,2}, L. Origlia², E. Dalessandro², E. Valenti³, M. Bellazzini², M. A. Tioncco⁴, A. L. Varri⁵, E. Vesperini⁴, and G. Beccari³

¹Dipartimento di Fisica e Astronomia, Università degli Studi di Bologna, via Gobetti 93/2, I-40129 Bologna, Italy

²INAF-Osservatorio di Astrofisica e Scienza dello Spazio di Bologna, Via Gobetti 93/3, I-40129, Bologna, Italy

³European Southern Observatory, Karl-Schwarzschild-Strasse 2, D-85748 Garching bei München, Germany

⁴Dept. of Astronomy, Indiana University, Bloomington, IN 47401, USA

⁵Institute for Astronomy, University of Edinburgh, Royal Observatory, Blackford Hill, Edinburgh EH9 3HJ, UK

Received 2018 March 29; revised 2018 April 27; accepted 2018 May 1; published 2018 June 26

Abstract

In the context of the ESO-VLT Multi-Instrument Kinematic Survey (MIKIS) of Galactic globular clusters (GGCs), we present the line-of-sight rotation curve and velocity dispersion profile of M5 (NGC 5904), as determined from the radial velocity of more than 800 individual stars observed out to 700'' (~ 5 half-mass radii) from the center. We found one of the cleanest and most coherent rotation patterns ever observed for globular clusters, with a very stable rotation axis (having constant position angle of 145° at all surveyed radii) and a well-defined rotation curve. The density distribution turns out to be flattened in the direction perpendicular to the rotation axis, with a maximum ellipticity of ~ 0.15 . The rotation velocity peak ($\sim 3 \text{ km s}^{-1}$ in projection) is observed at ~ 0.6 half-mass radii, and its ratio with respect to the central velocity dispersion ($\sim 0.3\text{--}0.4$ at 4 projected half-mass radii) indicates that ordered motions play a significant dynamical role. This result strengthens the growing empirical evidence of the kinematic complexity of GGCs and motivates the need of fundamental investigations of the role of angular momentum in collisional stellar dynamics.

Key words: globular clusters: individual (NGC 5904) – stars: kinematics and dynamics – techniques: spectroscopic

1. Introduction

Galactic globular clusters (GGCs) are ideal laboratories where the large variety of phenomena due to collisional stellar dynamics can be observationally studied. They have been always considered spherical, nonrotating, and almost completely relaxed stellar systems. Hence, simple isotropic and nonrotating models (King 1966) are usually adopted to reproduce their observed surface brightness/star count profiles and to derive their structural parameters (e.g., Harris 1996). However, recent N -body simulations indicate that GGCs do not attain complete energy equipartition (Trenti & van der Marel 2013; see also Bianchini et al. 2016), and they may show differential rotation and complex behaviors of pressure anisotropy, depending on the degree of dynamical evolution suffered and the effect of an external tidal field (e.g., Vesperini et al. 2014).

Also from the observational point of view, increasing evidence is demonstrating that these models are largely over-simplified. Indeed, deviations from the sharply truncated King phase space distribution (e.g., see the cases of NGC 1851, as studied by Olszewski et al. 2009; Marino et al. 2014, NGC 5694 by Correnti et al. 2011; Bellazzini et al. 2015, and several others, as discussed, e.g., by Carballo-Bello et al. 2018), spherical symmetry (e.g., Chen & Chen 2010), and pressure isotropy (e.g., van de Ven et al. 2006; Bellini et al. 2014, 2017; Watkins et al. 2015) are found in a growing number of GGCs. Also the observational evidence of systemic rotation is increasing (e.g., Anderson & King 2003; Lane et al. 2009, 2010; Bellazzini et al. 2012;

Bianchini et al. 2013; Fabricius et al. 2014; Kacharov et al. 2014; Kimmig et al. 2015; Lardo et al. 2015; Bellini et al. 2017; Boberg et al. 2017; Cordero et al. 2017; Ferraro et al. 2018b; Kamann et al. 2018), possibly suggesting that, when properly surveyed, the majority of GGCs rotate at some level. In particular, Ferraro et al. (2018b) investigated the intermediate/external region of 11 clusters, demonstrating the presence of internal rotation in almost all of them. Kamann et al. (2018) surveyed the central regions of 25 GGCs, detecting signals of rotation in 60% of their sample. On the other hand, recent N -body simulations (Tioncco et al. 2017) describing the long-term evolution of GC rotational properties suggest that the detection of (even modest) signals is crucial, as they may provide useful lower limits to the amount of angular momentum imprinted during their formation process.

As part of the ESO-VLT Multi-Instrument Kinematic Survey of GGCs (hereafter the MIKIS Survey; Ferraro et al. 2018b),⁶ here we present the line-of-sight internal kinematics of M5 (NGC 5904) obtained from the combination of FLAMES and KMOS data. With a total sample of more than 800 stars extending out to ~ 5 half-mass radii, the data set presented here allowed us to construct the most detailed rotation curve and velocity dispersion profile so far for the intermediate/outer regions of the system, clearly showing the presence of a coherent systemic rotation pattern. The paper is organized as follows. In Section 2, we describe the observational data set and the data reduction procedures adopted for the analysis. The determination of the RV from the acquired individual star

* Based on FLAMES and KMOS observations performed at the European Southern Observatory as part of the Large Programme 193.D-0232 (PI: Ferraro).

⁶ The MIKIS Survey was specifically designed to determine the entire velocity dispersion profile and rotation curve of 30 appropriately selected GGCs, from the radial velocity (RV) of hundreds of individual stars, measured thanks to the combination of three spectrographs (SINFONI+KMOS+FLAMES) mounted at the ESO Very Large Telescope (VLT).

Table 1
Summary of the FLAMES Data Sets

Program ID	Grating	PI	N	N_{com}
193.D-0232	HR21	(Ferraro)	477	
073.D-0695	HR5	(Recio Blanco)	57	5
088.B-0403	HR9	(Lucatello)	114	17
073.D-0211	HR11	(Carretta)	117	17
087.D-0230	HR12	(Gratton)	94	6
073.D-0211	HR13	(Carretta)	113	13
087.D-0276	HR15	(D’Orazi)	115	24

Note. The table lists the FLAMES data sets used to derive the internal kinematics of M5. The MICKS survey sample corresponds to program ID 193.D-0232, while the others have been retrieved from the ESO archive. The last two columns list the number of measured RVs in each program (N) and the number of stars in common with the MICKS survey sample (N_{com}).

spectra is discussed in Section 3. Section 4 is devoted to present the obtained results: the systemic RV of the system, its rotation curve and velocity dispersion profile, and the projected density map determined from resolved star photometry, from which we estimated the cluster ellipticity. The results are then discussed in Section 5.

2. Observations and Data Reduction

The observational strategy and the data reduction procedure adopted in the MICKS Survey are described in Ferraro et al. (2018b). Here, we schematically remind just the main points.

We used the spectrograph FLAMES/GIRAFFE/MEDUSA (Pasquini et al. 2000), which allows us to allocate 132 deployable fibers over a large ($25'$ -diameter) field of view. In particular, the adoption of grating HR21 (covering $\Delta\lambda = 8484\text{--}9001 \text{ \AA}$, with a resolving power $R \sim 16200$) allowed us to sample the Ca II triplet, which is an excellent feature to measure RVs. The target stars have been selected from *Hubble Space Telescope* ACS/WFC data acquired in the F606W and F814W bands (Sarajedini et al. 2007) and a complementary wide-field catalog in B and V obtained from ESO-WFI observations, as described in Lanzoni et al. (2007). They are located along the red giant, asymptotic giant and horizontal branches of the cluster, at magnitudes brighter than $V = 17.0$ (V_{ground} in the ACS catalog). To prevent the contamination of the target spectra from close sources, only stars without any bright neighboring object ($V_{\text{neighbor}} < V_{\text{star}} + 1.0$) within $2''$ have been selected. Five different pointings, with integration times ranging from 900 to 1800 s, were secured. In each exposure, typically 15–20 spectra of the sky were acquired; these have been averaged to obtain a master sky spectrum, which was then subtracted from the spectrum of each target. For homogeneization purposes, we re-observed ~ 30 stars already observed in previous campaigns (see Table 1). The standard data reduction (including bias-subtraction, flat-field correction, wavelength calibration, and extraction of one-dimensional spectra) was performed for both the MICKS Survey and the archive spectra, by using the FLAMES-GIRAFFE pipeline.⁷

Complementary observations with the spectrograph KMOS (equipped with 24 deployable $2''8 \times 2''8$ IF units, which can be allocated over a field of view of $7''2$ diameter; Sharples et al. 2010) were secured. We used the YJ grating (with $R \approx 3400$) covering the $1.00\text{--}1.35 \mu\text{m}$ spectral range. This

setup allows the observations of several reference telluric lines, thus ensuring an accurate RV calibration. The selected targets are red and asymptotic giant branch stars with $J < 14$ ($V < 16.8$), located within $\sim 145''$ from the cluster center. For a proper homogeneization of the RV measures, ~ 30 targets have been selected in common with the FLAMES data set. We secured 10 pointings with total integration times ranging from 30 to 100 s, depending on the target magnitudes. In order to perform a proper subtraction of the background, we observed an off-set sky field at several arcminutes from the cluster center. The standard pre-reduction procedure (including background subtraction, flat-field correction, and wavelength calibration of the two-dimensional spectra) was applied to the raw data by using the KMOS pipeline.³ Finally, we manually extracted the one dimensional spectrum from the brightest spaxel of each target star. The typical signal-to-noise ratio (S/N) is 50.

3. Radial Velocity Measurements

RVs were obtained as described in Ferraro et al. (2018b). In short, we followed the procedure discussed in Tonry & Davis (1979): the secured spectra were first corrected for heliocentric velocity, and then cross-correlated with a set of synthetic templates of known velocity, computed assuming appropriate metallicity and atmospheric parameters, by using the SYNTH code (see, e.g., Sbordone et al. 2004). The typical uncertainties in the RVs derived from FLAMES spectra (also including the wavelength calibration uncertainty estimated against sky lines) are of the order of $0.1\text{--}0.5 \text{ km s}^{-1}$. Uncertainties in the RVs derived from KMOS spectra were estimated via extensive Monte Carlo simulations, performing cross-correlation with synthetic spectra of appropriate metallicity, opportunely resampled at the KMOS pixel-scale, and with Poissonian noise added. We created 500 noisy spectra for different S/N values in the range between about 30 and 100. The RVs of these samples have been measured by using the cross-correlation technique adopted for the observed KMOS spectra, and the dispersion of the derived RVs has been assumed as the typical RV uncertainty (ϵ_{RV}) for the corresponding S/N. The derived relation between S/N and RV error is (see Figure 1): $\ln(\epsilon_{\text{RV}}) = 6.231 - 1.169 \ln(\text{S/N})$. The stars in common were used to report the KMOS and the archive measures to the MICKS RVs (determined from the HR21 grating). If multiple exposures were available for the same star, we adopted the RV obtained from the weighted mean of the higher resolution and higher quality measures, by using the individual errors as weights (hence, for all of the stars in common between the FLAMES and the KMOS data sets, we adopted the FLAMES values).

4. Results

4.1. Systemic Velocity

The final sample of RVs in the direction of M5 consists of 857 measures for individual sources distributed out to $727''$ from the cluster center. Adopting the values quoted in Miocchi et al. (2013), this corresponds to ~ 26 core radii ($r_c = 28''$) or 5 half-mass radii ($r_h = 140''$). The innermost star is at $r = 6''$, but only a dozen of measures are available within $15''\text{--}20''$ from the center because of the stellar crowding limitations. The distribution of RVs as a function of the distance from the center is plotted in Figure 2. Cluster

⁷ <http://www.eso.org/sci/software/pipelines/>

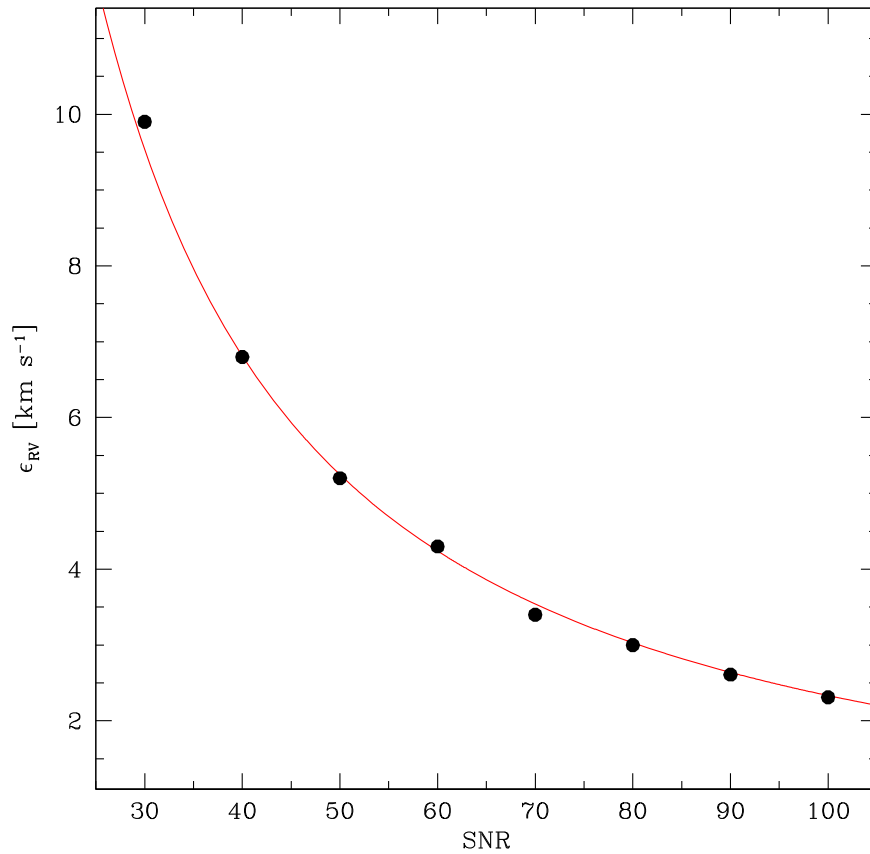


Figure 1. KMOS radial velocity uncertainties estimated through Monte Carlo simulations for different values of the S/N (see Section 3). Each circle is the rms dispersion of the RV measures obtained through cross-correlation against 500 noisy synthetic spectra with given S/N. The red line corresponds to the analytic curve quoted in Section 3.

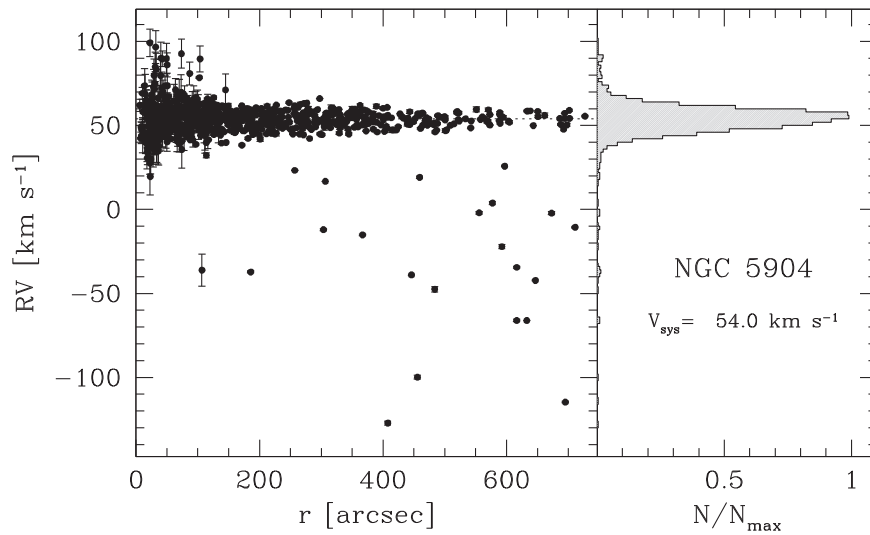


Figure 2. Left panel: observed radial velocities vs. cluster-centric distances, as obtained in this work. Right panel: histogram of the RV distribution, normalized to its peak value. The value of the derived systemic velocity of M5 is labeled.

members are easily identified, as they draw the distribution characterized by a clear peak and a small spread, while the Galactic field component is negligible at all radii. Assuming that the RV distribution is Gaussian, we used a maximum-likelihood approach (e.g., Walker et al. 2006) to estimate cluster systemic velocity and its uncertainty. For this purpose,

only the 677 RVs measured from FLAMES spectra have been used, and obvious outliers (as field stars) have been excluded from the analysis by means of a 3σ -clipping procedure. The resulting value of the cluster systemic velocity is $V_{\text{sys}} = 54.0 \pm 0.2 \text{ km s}^{-1}$, in good agreement with previous determinations (see Harris 1996; Kimmig et al. 2015). In the

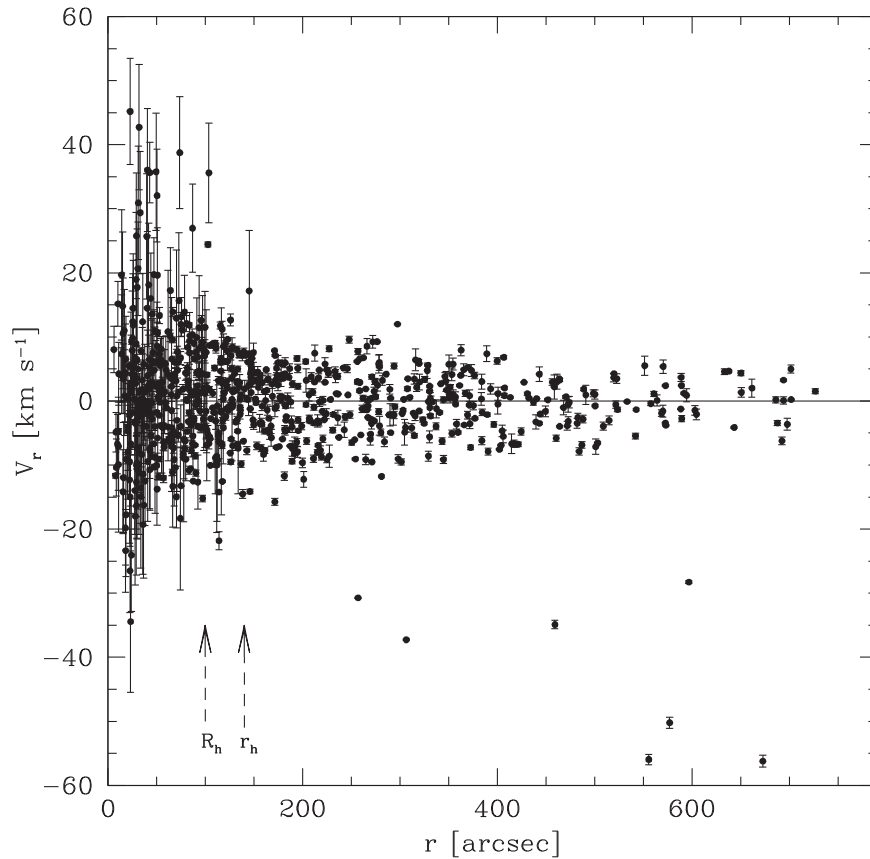


Figure 3. Zoomed view of the radial distribution of the measured velocities referred to V_{sys} . The large scatter observable at large distances from the cluster center is a clear signature of systemic rotation. The two arrows indicate the projected and the three-dimensional half-mass radii of M5 ($R_h = 100''$ and $r_h = 140''$, respectively; from Miocchi et al. 2013).

following, we will use V_r to indicate RVs referred to the cluster systemic velocity: $V_r \equiv \text{RV} - V_{\text{sys}}$.

4.2. Systemic Rotation

A zoomed view of V_r as a function of the distance from the center (Figure 3) clearly shows that at the outermost sampled radii (corresponding to $5 r_h$), the distribution remains broad about the cluster systemic velocity. This is not expected for an isotropic pressure-supported system, where the velocity dispersion formally decreases to zero in the outskirts. It can be explained, instead, as an effect of systemic rotation. Figure 4 shows the distribution of the surveyed stars on the plane of the sky (where x and y are the R.A. and decl. coordinates referred to those of the cluster center, adopted from Miocchi et al. 2013), with the red and the blue colors indicating, respectively, positive and negative values of V_r (i.e., RVs larger and smaller than the systemic velocity, respectively). As apparent from the figure, the evident prevalence of stars with positive values of V_r in the upper-left portion of the map and that of sources with $V_r < 0$ in the lower-right part of the diagram is a clear-cut signature of systemic rotation.

To investigate the rotation properties in this cluster, we used the same approach adopted in Ferraro et al. (2018b) and described, e.g., in Bellazzini et al. (2012, see also Lanzoni et al. 2013). The method consists in splitting the RV data set in two sub-samples with a line passing through the cluster center, and determining the difference between the mean velocity of the two groups (ΔV_{mean}). This is done by varying the position

angle (PA) of the splitting line from 0° (north direction) to 180° (south direction), by steps of 10° , and with 90° direction corresponding to the east. In the presence of rotation, ΔV_{mean} draws a coherent sinusoidal variation as a function of PA, its maximum absolute value providing twice the rotation amplitude (A_{rot}) and the position angle of the rotation axis (PA_0). The rotation of the standard coordinate system with respect to the cluster center (x, y) over the position angle PA_0 provides the rotated coordinate system (XR, YR), with XR set along the cluster major axis and YR aligned with the rotation axis. In a diagram showing V_r as a function of the projected distances from the rotation axis (XR), the stellar distribution shows an asymmetry, with two diagonally opposite quadrants being more populated than the remaining two. Moreover, the sub-samples of stars on each side of the rotation axis (i.e., with positive and with negative values of XR) have different cumulative V_r distributions and different mean velocities. To quantify the statistical significance of such differences, we used three estimators: the probability that the RV distributions of the two sub-samples are extracted from the same parent family is evaluated by means of a Kolmogorov–Smirnov test, while the statistical significance of the difference between the two sample means is estimated with both the Student’s t-test and a maximum-likelihood approach.

We applied this procedure to our RV sample in a set of concentric annuli around the cluster center, avoiding the innermost region ($r < 20''$), where the statistic is poor, and the outermost region ($r > 600''$), where the sampling is scant

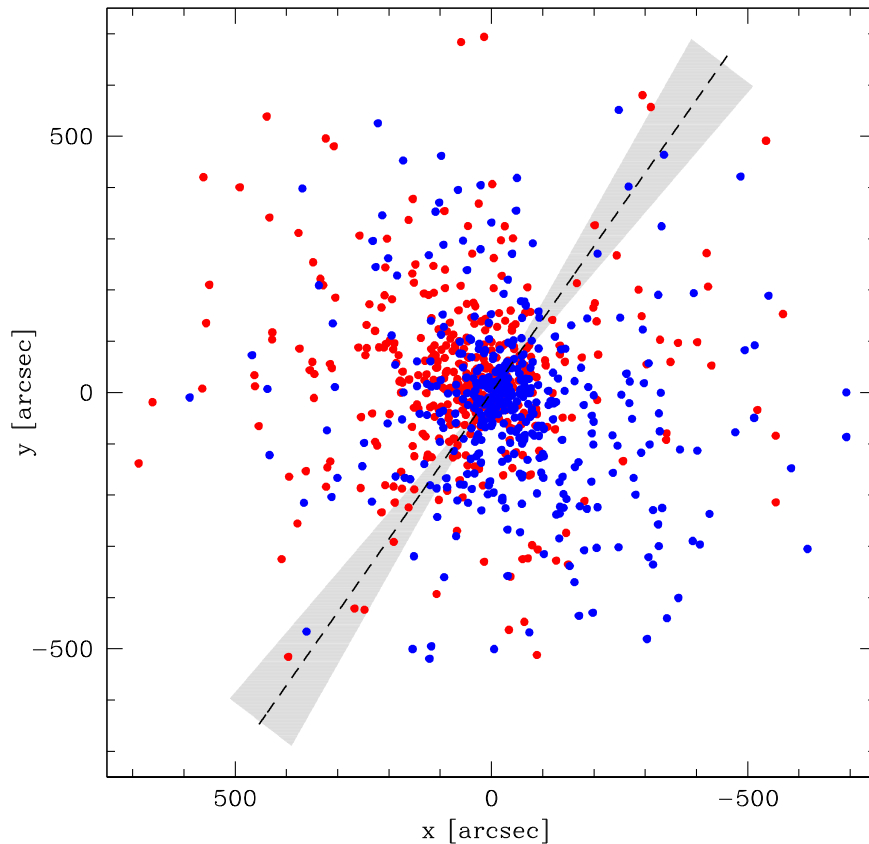


Figure 4. Distribution of the observed sample on the plane of the sky, with $x = (\text{R.A.} - \text{R.A.}_0) \cos(\text{decl.})$ and $y = \text{decl.} - \text{decl.}_0$ (R.A._0 and decl._0 being the coordinates of the cluster center, adopted from Mocchi et al. 2013). North is up, east is to the left. The colors distinguish stars with radial velocity larger than V_{sys} (in red), from those with $V_r < 0$ (in blue). The dashed line marks the position of the rotation axis, which has a position angle of 145° from north (as measured anti-clockwise). Its 1σ uncertainty region ($\pm 5^\circ.5$) is shaded in gray.

and nonsymmetric. The results are listed in Table 2 and plotted in Figures 5 and 6. In all of the considered annuli, we find well-defined sinusoidal behaviors of ΔV_{mean} as a function of PA (left-hand panels in Figures 5 and 6), asymmetric distributions of V_r as a function of the projected distance from the rotation axis XR (central panels), and well-separated cumulative V_r distributions for the two samples on either side of the rotation axis (right-hand panels). The reliability of these systemic rotation signatures is also confirmed by the values of the Kolmogorov–Smirnov and t-Student probabilities and by the significance level of different sample means obtained from the maximum-likelihood approach (see the three last columns in Table 2). Furthermore, as also shown in Figure 7, the position angle of the rotation axis (PA_0) is essentially constant in all of the investigated annuli, as expected in the case of a coherent global rotation of the system. To conservatively determine the best-fit position angle PA_0 of the global rotation of M5, we considered only the radial range ($r > 40''$) where statistically significant signatures are detected. We thus found $\text{PA}_0 = 145^\circ$. Its location in the plane of the sky (x, y) is shown as a dashed line in Figures 4 and 7. By fixing PA_0 to this value and using all of the observed stars, we finally obtain the diagnostic plots shown in Figure 8 and the values listed in Table 3 for the global rotation signatures of M5. A complementary analysis following the approach described in Kamann et al. (2018) fully confirms these results and provides a 1σ uncertainty of $5^\circ.5$ for the rotation axis position angle (see the shaded region in Figures 4 and 7). This is one of the strongest and cleanest evidences of rotation found to date in a GC.

Table 2
Rotation Signatures Detected in Circular Annuli around the Cluster Center

r_i	r_e	r_m	N	PA_0	A_{rot}	P_{KS}	P_{Stud}	$n-\sigma_{\text{ML}}$
20	40	29.4	89	163	2.3	7.500	>90.0	1.4
40	70	54.0	105	145	2.0	0.001	>99.8	4.2
70	110	88.8	118	144	2.3	1.051	>99.8	3.4
110	150	128.3	108	148	2.5	0.005	>99.8	3.9
150	220	182.0	111	151	1.9	0.015	>99.8	4.8
220	320	268.0	107	144	2.3	0.001	>99.8	4.7
320	600	426.2	141	145	1.4	0.313	>99.8	3.6

Note. For each annulus the table lists: the inner and outer radius (r_i and r_e) in arcseconds, the mean radius and the number of stars in the bin (r_m and N , respectively), the position angle of the rotation axis (PA_0), the rotation amplitude (A_{rot}), the probability, following the Kolmogorov–Smirnov statistics, that the two RV samples separated by the rotation axis are drawn from the same parent distribution (P_{KS}), the probability that the means of the two RV samples are different, following the t-Student test (P_{Stud}), and following a maximum-likelihood approach, with $n-\sigma_{\text{ML}}$ expressing the significance level of the difference.

4.3. Ellipticity

A rapidly rotating system also is expected to be flattened in the direction perpendicular to the rotation axis (Chandrasekhar 1969). To investigate this issue, we used the *HST*/ACS and ESO-WFI catalogs discussed above and built the stellar density map of the system. Only stars with $V < 19$ (~ 0.5 mag below the main sequence turn-off point) have been used to avoid

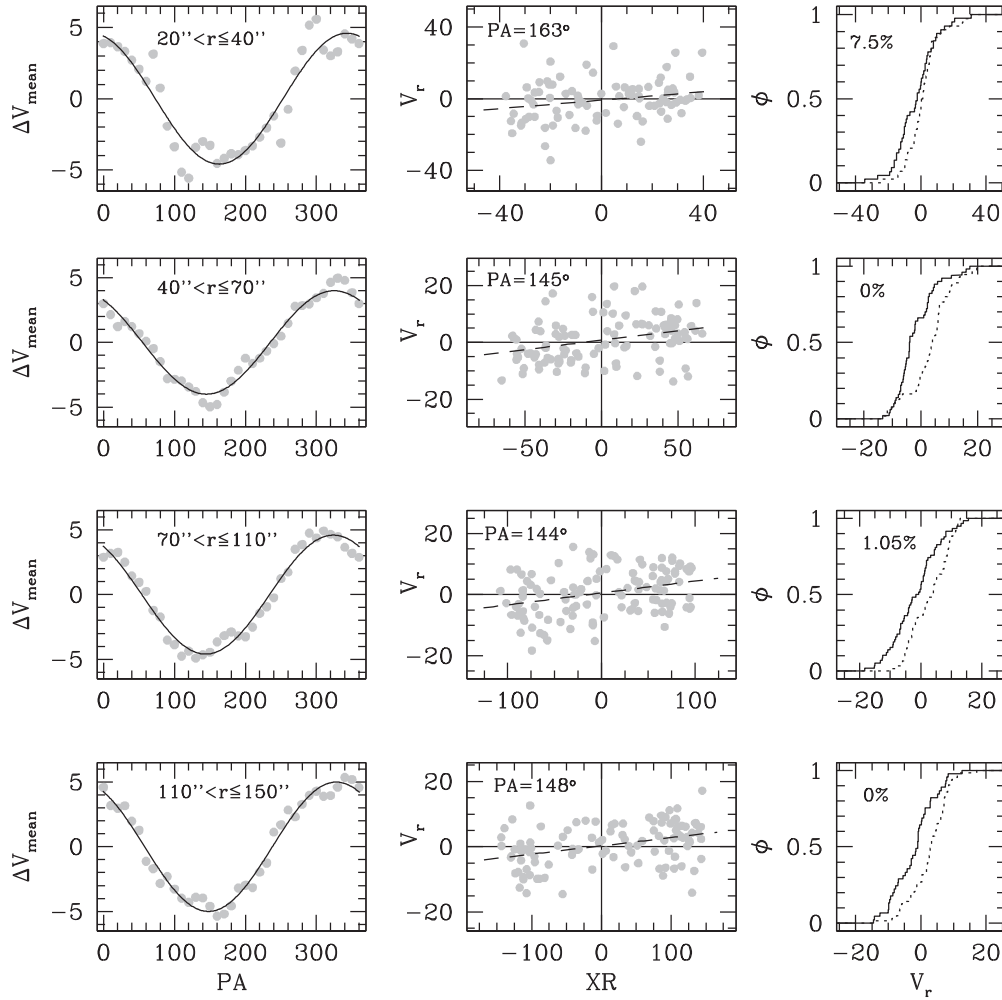


Figure 5. Diagnostic diagrams of the rotation signature detected in the first four concentric annuli listed in Table 2 (see labels in the left-hand panels). For each bin, the difference between the average RV of two samples divided by a line passing through the cluster center is shown as a function of line position angle (PA) in the left panel. The best-fit sine function is also shown as a solid line. In the central panel, we plot the line-of-sight velocities vs. the projected distances from the best-fit rotation axis (in arcseconds). The position angle of the rotation axis is labeled and the least square best-fit to the RV distribution is marked with a dashed line. The cumulative RV distributions for the two sets on either sides of the rotation axis (i.e., with $XR < 0$ and $XR > 0$) are shown in the right panel (solid and dotted lines, respectively), where we also labeled their Kolmogorov–Smirnov probability to be drawn from the same parent family.

incompleteness effects. This allowed us to extend the analysis out to $\sim 200''$. The resulting map is shown in Figure 9, where the dashed straight line marks the position of the rotation axis, the black solid lines draw the isodensity contours, and the white lines correspond to their best-fit ellipses. These latter have been determined by following the iterative procedure described in Jędrzejewski (1987). The resulting values of the ellipticity as a function of the distance along the major axis XR are shown in Figure 10. As apparent, the stellar density distribution has spherical symmetry in the center and becomes increasingly flattened in the direction perpendicular to the rotation axis for increasing radius. Qualitatively, this trend is consistent with the model predictions of stellar systems flattened by rotation (e.g., Lupton & Gunn 1987; Varri & Bertin 2012) and found in the observational study of 47 Tucanae (Bianchini et al. 2013; Bellini et al. 2017; Heyl et al. 2017). For the two outermost ellipses shown in the figure (at $r \sim 80''$ and $r \sim 120''$), we measure $1 - b/a = 0.1$ and 0.14 , where a and b are the major and the minor axes, respectively.

4.4. Rotation Curve and Velocity Dispersion Profile

To determine the rotation curve of M5, we considered the rotated coordinate system (XR, YR) and split the V_r sample in five intervals of XR on both sides of the rotation axis. According to Walker et al. (2006, see also Martin et al. 2007; Sollima et al. 2009), we used the maximum-likelihood method to determine the mean velocity of all the stars belonging to each XR bin. To estimate the errors we followed Pryor & Meylan (1993). The resulting rotation curve (Figure 11 and Table 4) clearly shows the expected shape, with an increasing trend in the innermost regions up to a maximum value, and a decreasing behavior outward. The analytic expression (Lynden-Bell 1967) appropriate for cylindrical rotation

$$V_{\text{rot}} = \frac{2A_{\text{peak}}}{XR_{\text{peak}}} \frac{XR}{1 + (XR/XR_{\text{peak}})^2} \quad (1)$$

very well reproduces the observed rotation curve (see the red solid line in Figure 11), with a maximum amplitude of $\sim 3 \text{ km s}^{-1}$ at $\sim 90''$ from the rotation axis.

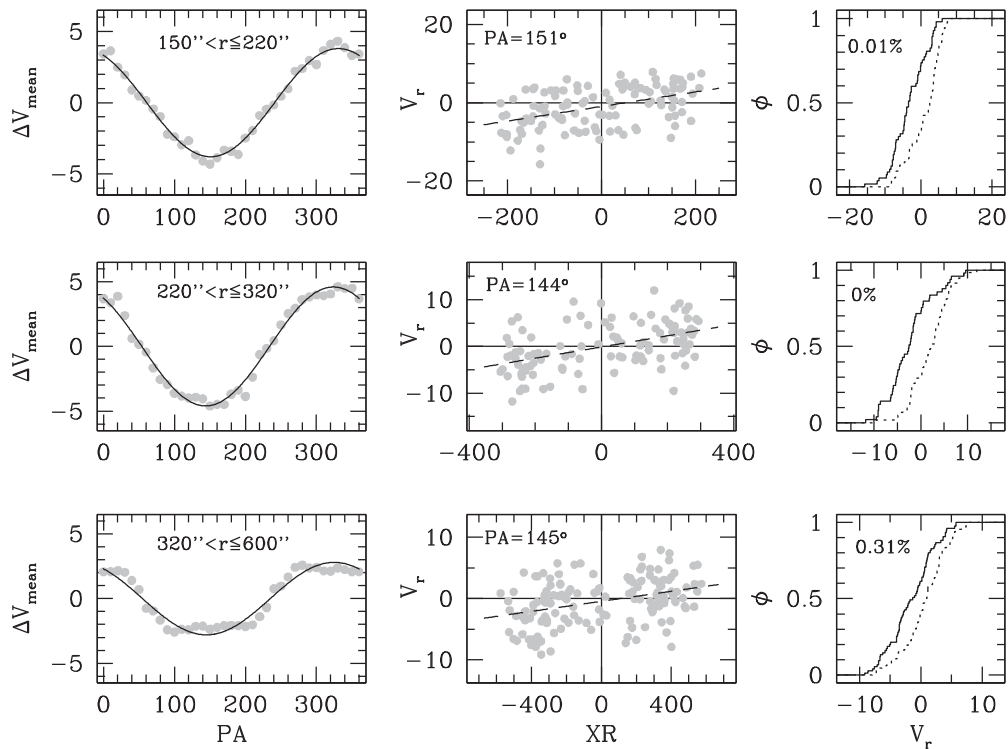


Figure 6. As in Figure 5, but for the three outermost considered annuli (see the labels in the left-hand panels).

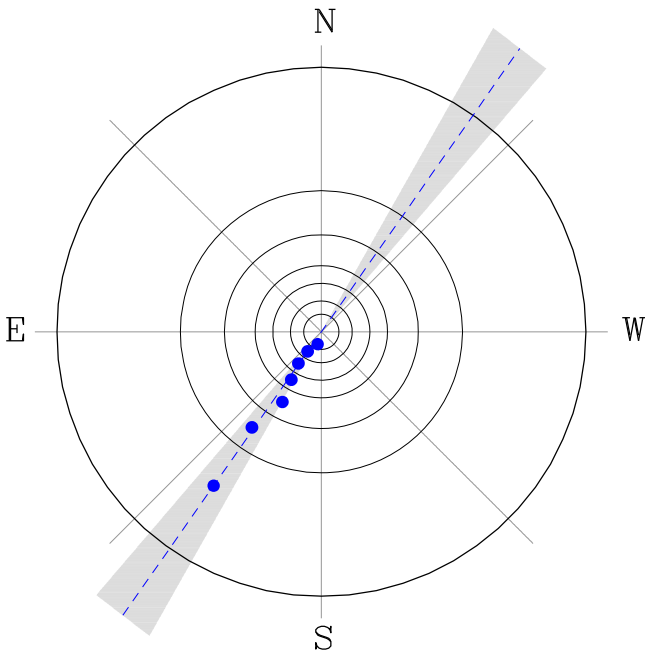


Figure 7. Position angle of the rotation axis in the radial bins listed in Table 2, used to search for rotation signatures (blue circles). As apparent, the value of PA is constant in all bins. The dashed line marks the direction of the adopted rotation axis of M5 (with position angle of $PA_0 = 145^\circ$, as measured anticlockwise from north to south). The shaded gray region shows the 1σ uncertainty interval ($\pm 5.5^\circ$) of PA_0 .

By folding the two RV samples on either side of the rotation axis and using the same five intervals of XR adopted for the rotation curve, we obtained the projected velocity dispersion profile shown in the left-hand panel of Figure 12 and listed in

the last two columns of Table 4. We emphasize that the velocity dispersion profiles most commonly shown in the literature are determined in circular annuli around the cluster center, rather than in shells of projected radial distances from the rotation axis (XR), as done in this figure. However, in the presence of a clear global rotation of the system, it is reasonable to assume cylindrical symmetry and thus to show the kinematical properties in the rotated coordinate system (XR, YR). Indeed, this allows a direct comparison with the rotation velocity (Figure 11), which is determined in the same projection. This comparison clearly shows that, in spite of a clean and relatively strong rotation, M5 is still dominated by nonordered motions at all distances from the rotation axis: in fact, the velocity dispersion is larger than the rotation velocity in all of the considered bins.

The projected velocity dispersion profile of M5 obtained in circular concentric shells is shown in the right-hand panel of Figure 12 (black circles) and listed in Table 5. This has been determined after subtracting from the measured RV of each star, the mean velocity of the XR shell to which the star belongs. For the sake of illustration, we also show the radial profile of second velocity moment (gray circles), i.e., the dispersion of the RVs measured within each circular bin, with no subtraction of the rotational component. Of course, the velocity dispersion is smaller than the second velocity moment in every bin. However, the differences are small and always within the errors, as expected in the case of a pressure-supported system. The comparison between the left-hand panel and the right-hand panel (black circles) of Figure 12 clearly shows that the central values of the velocity dispersion obtained by using XR shells are smaller than those determined in circular annuli. This is due to the fact that, by construction, the inner XR shells include stars that are spatially close to the rotation axis, but orbit both in the cluster central regions

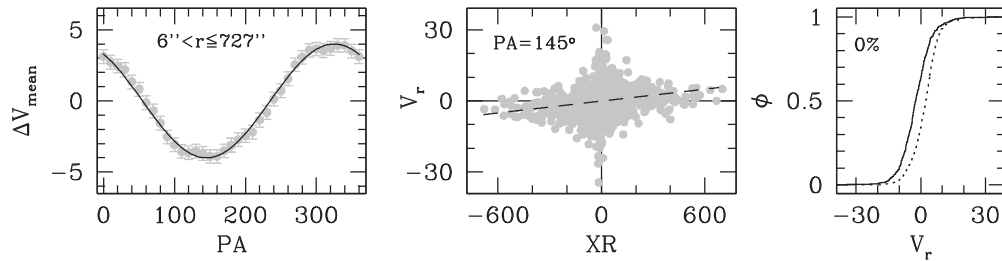


Figure 8. Diagnostic diagrams of the global rotation of M5. The meaning of each panel is as in Figures 5 and 6, but here we plot all of the observed stars (with cluster-centric distances $6'' < r \lesssim 727''$), assuming $PA_0 = 145^\circ$ as position angle of the rotation axis.

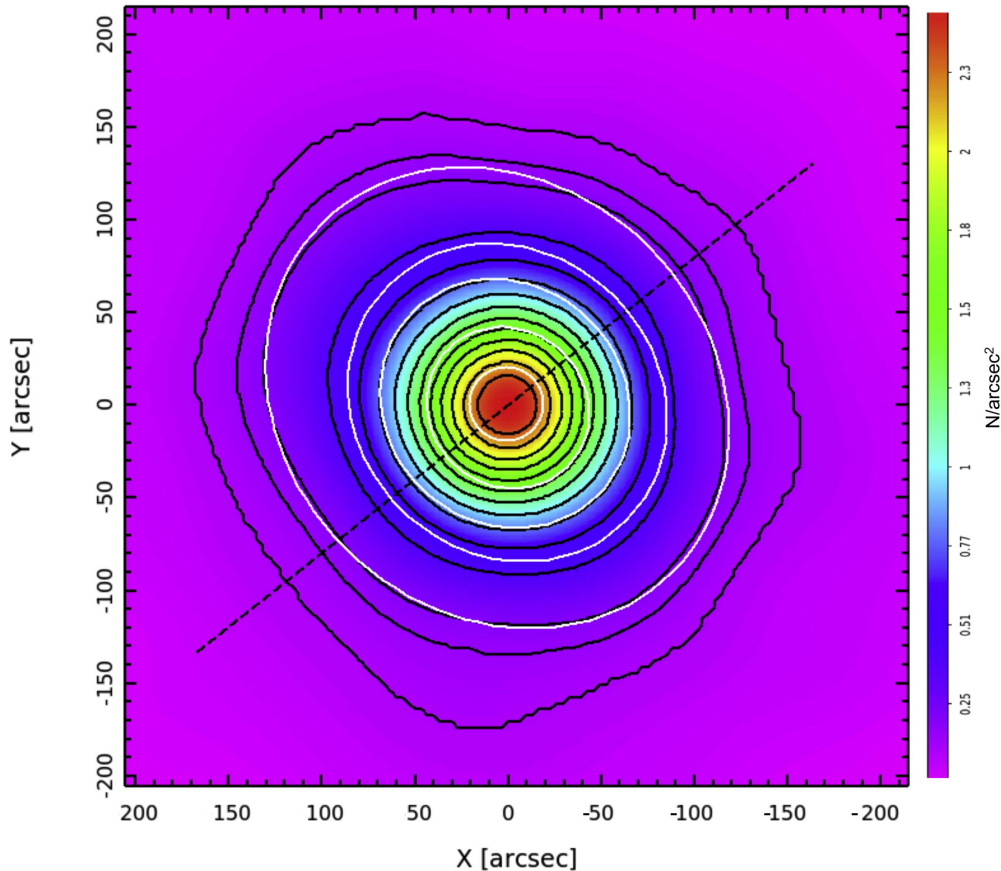


Figure 9. Stellar density map (number of stars per square arcsecond: see the color-bar) of the inner $200'' \times 200''$ of M5, obtained from *HST*/ACS and ESO-WFI photometry. The solid black lines are isodensity contours, the white curves are their best-fit ellipses. The black dashed line marks the direction of the global rotation axis (with position angle of 145°).

Table 3
Global Rotation Signature in MS

r_i	r_e	r_m	N	PA_0	A_{rot}	P_{KS}	P_{Stud}	$n-\sigma_{\text{ML}}$
6	727	186.3	823	145	2.0	0.000	>99.8	9.9

Note. The same as in Table 2, but for the entire radial range ($6''$ – $727''$) covered by the observations and after fixing the position angle of the rotation axis to $PA_0 = 145^\circ$.

(hence, with large velocity dispersion) and at the cluster periphery (hence, with small velocity dispersion). The innermost circular annulus, instead, is largely dominated by stars that are truly orbiting close to the center, and the “dilution” effect due to physically distant stars is much smaller.

As our observations extend out $\sim 10'$ away from the center, the projection of the cluster space motion along the line of sight could produce a nonnegligible amount of apparent rotation. To estimate the contribution of such perspective rotation to the true rotational velocity of M5, we followed the procedure described in van de Ven et al. (2006), adopting the values quoted in Narloch et al. (2017) for the systemic proper motion of M5. We found a mild variation of the position angle of the rotation axis ($PA_0 = 141^\circ$, instead of 145°) and values of V_{rot} and σ_P in very good agreement (well within the errors) with those quoted in Table 4. These results and the fact that updated values of the cluster proper motion will become available soon (thanks to the upcoming *Gaia* second data release), we decide not to apply perspective rotation corrections to our determinations.

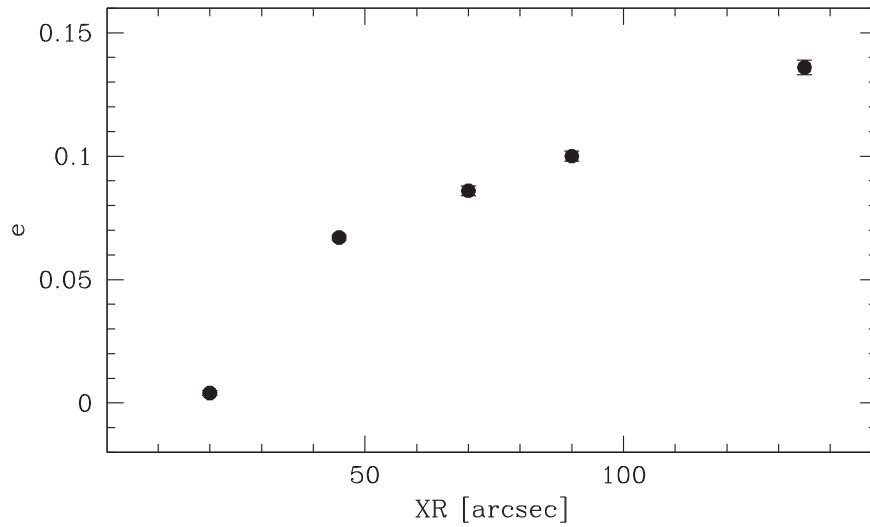


Figure 10. Observed ellipticity of M5 as a function of the distance from the center along the major axis XR, measured for the same best-fit ellipses plotted in white in Figure 9.

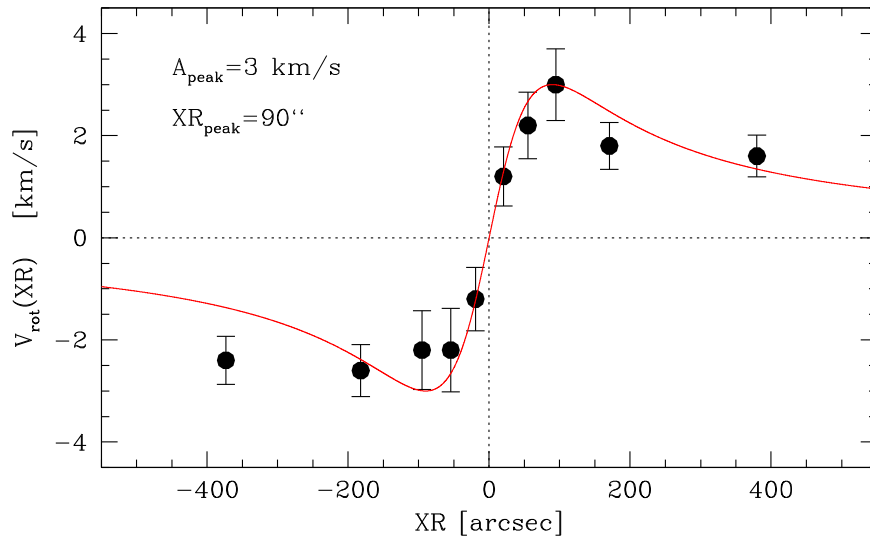


Figure 11. Rotation curve of M5. The black circles mark the stellar mean velocity as a function of the projected distance on either side of the rotation axis (XR) for the intervals listed in Table 4. The red line, which well reproduces the observed curve, has the functional form expressed in Equation (1), with $A_{\text{peak}} = 3 \text{ km s}^{-1}$ and $\text{XR}_{\text{peak}} = 90''$.

Table 4
Rotation Curve and Folded Velocity Dispersion Profile of M5 in the Rotated System (XR, YR)

XR_i	XR_e	XR_{m+}	N_+	$V_{\text{rot}+}$	ϵ_{V+}	XR_{m-}	N_-	$V_{\text{rot}-}$	ϵ_{V-}	$\sigma_p(\text{XR})$	$\epsilon_{\sigma p}$
0	40	20.2	131	1.2	0.6	-19.3	134	-1.2	0.6	5.9	0.3
40	70	55.0	69	2.2	0.6	-54.3	55	-2.2	0.8	5.4	0.4
70	120	94.6	64	3.0	0.7	-95.2	65	-2.2	0.8	5.6	0.4
120	250	170.6	91	1.8	0.5	-182.1	79	-2.6	0.5	4.4	0.2
250	727	379.9	65	1.6	0.4	-373.3	65	-2.4	0.5	3.4	0.2

Note. For five intervals of projected distances from the rotation axis (XR), the table lists: the inner and outer absolute limits of each bin (XR_i and XR_e) in arcseconds, the mean distance, number of stars, average velocity and its error (in km s^{-1}) on the positive side of the XR axis (Columns 3–6), the same for the negative side of the XR Axis (Columns 7–10), and the folded velocity dispersion and its error (Columns 11–12).

5. Discussion

As part of the ESO-VLT MICKS Survey (Ferraro et al. 2018b), we presented solid and unambiguous evidence of strong global rotation between $\sim 0.5r_h$ and $5r_h$ in the GGC M5. Signatures of systemic rotation in this system, both in the outskirts and in the central regions, were already presented in

previous works. Bellazzini et al. (2012) found a rotation signal, with an amplitude of 2.6 km s^{-1} and a position angle of 157° , from the analysis of 136 individual star spectra at $\sim 60'' < r < 600''$. From a sample of 128 stars distributed between $\sim 70''$ and $\sim 1400''$, Kimmig et al. (2015) report an amplitude of 2.1 km s^{-1} . Fabricius et al. (2014) performed an

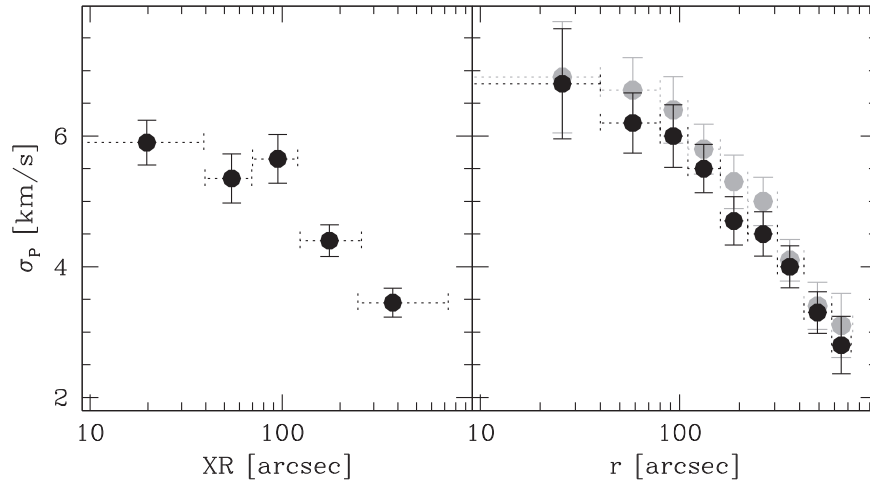


Figure 12. Velocity dispersion profile of M5 obtained in two different projections. Left-hand panel: folded velocity dispersion profile determined in the same shells of projected distance from the rotation axis (XR) used for the rotation curve plotted in Figure 11. The corresponding values and error bars are listed in the last two columns of Table 4. Right-hand panel: velocity dispersion profile obtained in concentric circular annuli around the cluster center (solid circles; see also Table 5). For the sake of illustration, we also show the profile of the second velocity moment, which includes the effects of both rotation and velocity dispersion in each circular shell (gray circles and last two columns in Table 5).

Table 5
Velocity Dispersion and Second Velocity Moment Profiles of M5

r_i	r_e	r_m	N	$\sigma_p(r)$	ϵ_σ	$\tilde{\sigma}_p(r)$	$\epsilon_{\tilde{\sigma}}$
6	40	25.8	116	6.8	0.8	6.9	0.9
40	80	58.2	132	6.2	0.5	6.7	0.5
80	110	93.0	91	6.0	0.5	6.4	0.5
110	160	132.2	126	5.5	0.4	5.8	0.4
160	220	187.2	93	4.7	0.4	5.3	0.4
220	310	262.5	96	4.5	0.3	5.0	0.4
310	420	357.6	88	4.0	0.3	4.1	0.3
420	580	492.5	58	3.3	0.3	3.4	0.4
580	727	648.3	23	2.8	0.4	3.1	0.5

Note. Internal and external radius of each annulus in arcseconds (columns 1, 2); average cluster-centric distance and number of stars in the bin (columns 3, 4); projected velocity dispersion (km s⁻¹) and its uncertainty (columns 5, 6); projected second velocity moment and its uncertainty (columns 7, 8).

integrated-light spectroscopic study of the innermost $\sim 60'' \times 60''$ of M5, finding a central velocity gradient of 2.1 km s^{-1} and a position angle of the rotation axis of 148.5° (once reported in the coordinate system adopted here). Very recently, Kamann et al. (2018) analyzed a large number of individual star spectra acquired at $r < 60''$ with the integral-field spectrograph ESO-MUSE, and found a velocity gradient of 2.2 km s^{-1} . They measured the rotation axis position angle in different radial bins around the cluster center, finding $\text{PA}_0 \sim 130^\circ\text{--}140^\circ$ (once reported in our system) at $r > 10''$, while the axis seems to be rotated by 90° in the innermost region. Although a detailed comparison of the rotation amplitude among the various works is not straightforward (because of the different radial regions sampled and/or the different parameters adopted to quantify it), typical values of $\sim 2 \text{ km s}^{-1}$ are found in all the studies. A very good agreement is also found for what concerns the position angle of the rotation axis. The only exception is the perpendicular direction found by Kamann et al. (2018) in the innermost $10''$ of the cluster. Higher spatial-resolution spectroscopy, with the enhanced version of MUSE operating at

super-seeing conditions, or with the adaptive-optics corrected spectrograph ESO-SINFONI (see Lanzoni et al. 2013), will shed new light on this intriguing feature.

With respect to previous works, our study has the advantage of being based on a much larger statistics at $r > 60''$. Hence, with the exception of the central region, it provides the most solid and precise determination of the rotation axis, rotation curve, and velocity dispersion profile of M5. Indeed, Figure 7 probably shows the cleanest evidence so far of a constant value of PA_0 with radius, testifying a coherent rotation and a reliable determination of the central kinematics of this cluster. The resulting rotation curve is illustrated in Figure 11. This profile is well reproduced by the analytic expression presented in Equation (1), which is appropriate for cylindrical rotation and is inspired by the structure of the velocity space of stellar systems resulting from the process of violent relaxation (Lynden-Bell 1967; Gott 1973). The observed peak rotation amplitude is $A_{\text{peak}} \sim 3 \text{ km s}^{-1}$ and is located at about $0.6 r_h$ from the center. The radial distribution of the angular momentum is such that the behavior in the central regions is consistent with solid-body rotation, while in the outer portion of the radial range under consideration, it declines smoothly. Of course, kinematic information along the line of sight provides exclusively a lower limit to the three-dimensional (3D) rotation content, due to projection effects.

To study the relative importance of ordered versus random motions and to quantify the role of rotation in shaping the geometry of a stellar system, the ratio between the peak rotational velocity and the central velocity dispersion is commonly used (for recent studies, see, e.g., Bianchini et al. 2013; Kacharov et al. 2014; Jeffreson et al. 2017). As our data do not sample the inner region of M5, we adopt the central velocity dispersion $\sigma_0 = 7.3 \text{ km s}^{-1}$ quoted by Kamann et al. (2018), finding $V_{\text{peak}}/\sigma_0 = 0.4$. As discussed in Section 4.3, we adopt $e = 0.14$ for the cluster ellipticity. In a plot of V_{peak}/σ_0 versus the ellipticity, M5 is the GC with largest rotational support that exactly locates on the line of isotropic oblate rotators viewed edge-on (see, e.g., Figure 14 in Bianchini et al. 2013). Hence, on the basis of this simple argument, we suggest that the observed

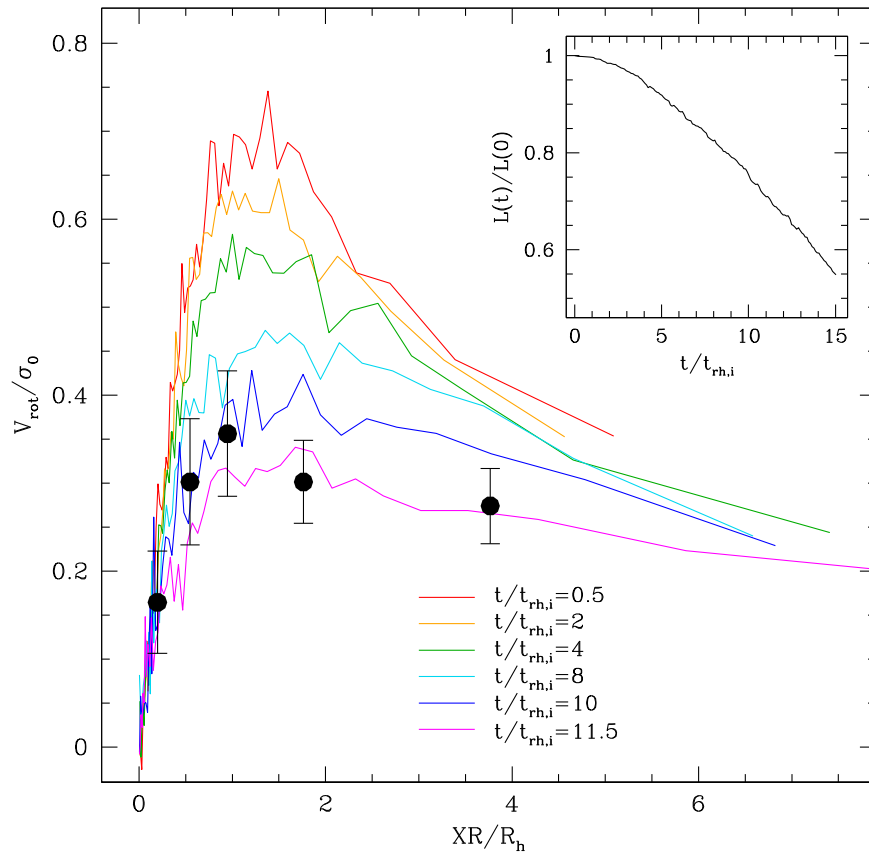


Figure 13. Time evolution of the radial profile of V_{rot}/σ_0 from one of the N -body simulations of Tiongco et al. (2016, the VBrotF04 model, see their Table 1). The radial distances from the rotation axis (XR) are expressed in units of the projected half-mass-radius ($R_h = 100''$; from Miocchi et al. 2013). An inclination angle between the line of sight and the rotation axis of 20° is assumed in the calculation of the radial profiles. Each line shows the radial profile of V_{rot}/σ_0 calculated at different times (see labels, where $t_{\text{rh},i}$ is the cluster’s initial half-mass relaxation time). Each profile is calculated by combining three snapshots around the desired time. The black filled circles show the observed radial profile of M5: each point is the average of the V_{rot} values determined on the two sides of the rotation axis (see Table 4), normalized to the central velocity dispersion from Kamann et al. (2018). The inset shows the time evolution of the cluster’s total angular momentum (L), normalized to its initial value.

rotation amplitude is likely close to the 3D one (i.e., the stellar system is observed on a line of sight that is close to the edge-on projection), and the flattening of this cluster could be explained by its own internal rotation.

In a forthcoming article, we will present a complete investigation based on a global, self-consistent, axisymmetric dynamical model, characterized by differential rotation and anisotropy in the velocity space (e.g., Varri & Bertin 2012), coupled with appropriate N -body simulations (e.g., Tiongco et al. 2016, 2017, 2018). Nonetheless, here we present a first comparison between the radial profile of the ratio V_{rot}/σ_0 and the time evolution of such a kinematic observable, as resulting from a representative N -body model from the survey recently conducted by Tiongco et al. (2016, 2018). Such a comparison, which is illustrated in Figure 13, supports the conclusion that M5 has already experienced the effects of two-body relaxation and angular momentum transport over the course of several initial half-mass relaxation times ($t_{\text{rh},i}$). This simple analysis should be intended only as a proof-of-concept that, in most cases, the angular momentum measured in present-day GCs represent a lower limit of the amount they possessed at birth (for the time evolution of the total angular momentum of the model, see the figure inset). We wish to emphasize that this comparison did not require any ad-hoc tailoring of the initial conditions of the N -body model and exclusively involved a simple exploration of the projected observables over different







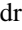

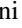



lines-of-sight. The inclination angle adopted in the figure (20°) is in qualitative agreement with the conclusion of an nearly edge-on view of the system discussed above. However, this value should be considered only as a representative example of a range of acceptable values, while a definitive assessment requires a full investigation of the degeneracy between intrinsic rotation and projection effects, which will be presented in the forthcoming dynamical study.

Rotation patterns as clear as those found in M5 have been detected just in a few other cases so far (see the cases of NGC 4372 in Kacharov et al. 2014, and 47 Tucanae in Bellini et al. 2017). However, evidence of systemic rotation signatures is mounting, with the most recent results for nine GCs presented in Ferraro et al. (2018a; but see also Bellazzini et al. 2012; Fabricius et al. 2014; Kacharov et al. 2014; Kimmig et al. 2015; Bellini et al. 2017; Boberg et al. 2017; Kamann et al. 2018, and references therein). As shown by a number of theoretical studies (e.g., Fiestas et al. 2006; Tiongco et al. 2017; see also Figure 13), internal dynamical evolution and stellar escape cause a gradual loss of the initial cluster internal rotation. Hence, any present-day detection likely is only a fraction of the system primordial rotation. Once combined with independent measures of the level of dynamical evolution determined, e.g., from the radial distribution of blue straggler stars (see Ferraro et al. 2009, 2012, 2018a; Lanzoni et al. 2016; Raso et al. 2017), these signals may be used to

clarify the formation and evolutionary histories of GCs, and the relative role of rotation. This outlook substantiates the urgency of multi-spectrograph studies of Galactic GCs (as the MIKIS Survey) sensible enough to detect even weak rotation signals in these systems. It also motivates the investment of renewed energies in the theoretical investigation of the role of angular momentum in collisional stellar dynamics, with appropriate equilibrium and evolutionary dynamical models.

We thank the anonymous referee for useful comments that helped improving the presentation of the paper. F.R.F. acknowledges the ESO Visitor Programme for the support and the warm hospitality at the ESO Headquarter in Garching (Germany) during the period when part of this work was performed. A.L.V. acknowledges support from a Marie Skłodowska-Curie Fellowship (MSCA-IF-EFRI 658088).

ORCID iDs

B. Lanzoni  <https://orcid.org/0000-0001-5613-4938>
 F. R. Ferraro  <https://orcid.org/0000-0002-2165-8528>
 A. Mucciarelli  <https://orcid.org/0000-0001-9158-8580>
 C. Pallanca  <https://orcid.org/0000-0002-7104-2107>
 E. Lapenna  <https://orcid.org/0000-0002-7662-2186>
 L. Origlia  <https://orcid.org/0000-0002-6040-5849>
 E. Dalessandro  <https://orcid.org/0000-0003-4237-4601>
 E. Valenti  <https://orcid.org/0000-0002-6092-7145>
 M. Bellazzini  <https://orcid.org/0000-0001-8200-810X>
 A. L. Varri  <https://orcid.org/0000-0002-6162-1594>
 E. Vesperini  <https://orcid.org/0000-0003-2742-6872>
 G. Beccari  <https://orcid.org/0000-0002-3865-9906>

References

- Anderson, J., & King, I. R. 2003, *AJ*, 126, 772
 Bellazzini, M., Bragaglia, A., Carretta, E., et al. 2012, *A&A*, 538, A18
 Bellazzini, M., Mucciarelli, A., Sollima, A., et al. 2015, *MNRAS*, 446, 3130
 Bellini, A., Anderson, J., van der Marel, R. P., et al. 2014, *ApJ*, 797, 115
 Bellini, A., Bianchini, P., Varri, A. L., et al. 2017, *ApJ*, 844, 167
 Bianchini, P., van de Ven, G., Norris, M. A., Schinnerer, E., & Varri, A. L. 2016, *MNRAS*, 458, 3644
 Bianchini, P., Varri, A. L., Bertin, G., & Zocchi, A. 2013, *ApJ*, 772, 67
 Boberg, O. M., Vesperini, E., Friel, E. D., Tiongco, M. A., & Varri, A. L. 2017, *ApJ*, 841, 114
 Carballo-Bello, J. A., Martínez-Delgado, D., Navarrete, C., et al. 2018, *MNRAS*, 474, 683
 Chandrasekhar, S. 1969, The Silliman Foundation Lectures (New Haven, CT: Yale Univ. Press)
 Chen, C. W., & Chen, W. P. 2010, *ApJ*, 721, 1790
 Cordero, M. J., Hénault-Brunet, V., Pilachowski, C. A., et al. 2017, *MNRAS*, 465, 3515
 Correnti, M., Bellazzini, M., Dalessandro, E., et al. 2011, *MNRAS*, 417, 2411
 Fabricius, M. H., Noyola, E., Rukdee, S., et al. 2014, *ApJL*, 787, L26
 Ferraro, F. R., Beccari, G., Dalessandro, E., et al. 2009, *Natur*, 462, 1028
 Ferraro, F. R., Lanzoni, B., Dalessandro, E., et al. 2012, *Natur*, 492, 393
 Ferraro, F. R., Lanzoni, B., Raso, S., et al. 2018a, *ApJ*, in press (arXiv:1805.00968)
 Ferraro, F. R., Mucciarelli, A., Lanzoni, B., et al. 2018b, *ApJ*, in press (arXiv:1804.08618)
 Fiestas, J., Spurzem, R., & Kim, E. 2006, *MNRAS*, 373, 677
 Gott, R. J., III 1973, *ApJ*, 186, 481
 Harris, W. E. 1996, *AJ*, 112, 1487
 Heyl, J., Caiazzo, I., Richer, H., et al. 2017, *ApJ*, 850, 186
 Jedrzejski, R. I. 1987, *MNRAS*, 226, 747
 Jeffreson, S. M. R., Sanders, J. L., Evans, N. W., et al. 2017, *MNRAS*, 469, 4740
 Kacharov, N., Bianchini, P., Koch, A., et al. 2014, *A&A*, 567, A69
 Kamann, S., Husser, T.-O., Dreizler, S., et al. 2018, *MNRAS*, 473, 5591
 Kimmig, B., Seth, A., Ivans, I. I., et al. 2015, *AJ*, 149, 53
 King, I. R. 1966, *AJ*, 71, 64
 Lane, R. R., Kiss, L. L., Lewis, G. F., et al. 2009, *MNRAS*, 400, 917
 Lane, R. R., Kiss, L. L., Lewis, G. F., et al. 2010, *MNRAS*, 406, 2732
 Lanzoni, B., Dalessandro, E., Ferraro, F. R., et al. 2007, *ApJ*, 663, 267
 Lanzoni, B., Ferraro, F. R., Alessandrini, E., et al. 2016, *ApJL*, 833, L29
 Lanzoni, B., Mucciarelli, A., Origlia, L., et al. 2013, *ApJ*, 769, 107
 Lardo, C., Pancino, E., Bellazzini, M., et al. 2015, *A&A*, 573, A115
 Lupton, R. H., & Gunn, J. E. 1987, *AJ*, 93, 1106
 Lynden-Bell, D. 1967, *MNRAS*, 136, 101
 Marino, A. F., Milone, A. P., Yong, D., et al. 2014, *MNRAS*, 442, 3044
 Martin, N. F., Ibata, R. A., Chapman, S. C., Irwin, M., & Lewis, G. F. 2007, *MNRAS*, 380, 281
 Mocchi, P., Lanzoni, B., Ferraro, F. R., et al. 2013, *ApJ*, 774, 151
 Narloch, W., Kaluzny, J., Poleski, R., et al. 2017, *MNRAS*, 471, 1446
 Olszewski, E. W., Saha, A., Knezek, P., et al. 2009, *AJ*, 138, 1570
 Pasquini, L., Avila, G., Allaert, E., et al. 2000, *Proc. SPIE*, 4008, 129
 Pryor, C., & Meylan, G. 1993, in ASP Conf. Ser. 50, Structure and Dynamics of Globular Clusters 50, ed. S. G. Djorgovski & G. Meylan (San Francisco, CA: ASP), 357
 Raso, S., Ferraro, F. R., Dalessandro, E., et al. 2017, *ApJ*, 839, 64
 Sarajedini, A., Bedin, L. R., Chaboyer, B., et al. 2007, *AJ*, 133, 1658
 Sbordone, L., Bonifacio, P., Castelli, F., & Kurucz, R. L. 2004, *MSAIS*, 5, 93
 Sharples, R., Bender, R., Agudo Berbel, A., et al. 2010, *Msngr*, 139, 24
 Sollima, A., Bellazzini, M., Smart, R. L., et al. 2009, *MNRAS*, 396, 2183
 Tiongco, M. A., Vesperini, E., & Varri, A. L. 2016, *MNRAS*, 461, 402
 Tiongco, M. A., Vesperini, E., & Varri, A. L. 2017, *MNRAS*, 469, 683
 Tiongco, M. A., Vesperini, E., & Varri, A. L. 2018, *MNRAS*, 475, L86
 Tonry, J., & Davis, M. 1979, *AJ*, 84, 1511
 Trenti, M., & van der Marel, R. 2013, *MNRAS*, 435, 3272
 van de Ven, G., van den Bosch, R. C. E., Verolme, E. K., & de Zeeuw, P. T. 2006, *A&A*, 445, 513
 Varri, A. L., & Bertin, G. 2012, *A&A*, 540, A94
 Vesperini, E., Varri, A. L., McMillan, S. L. W., & Zepf, S. E. 2014, *MNRAS*, 443, L79
 Walker, M. G., Mateo, M., Olszewski, E. W., et al. 2006, *AJ*, 131, 2114
 Watkins, L. L., van der Marel, R. P., Bellini, A., & Anderson, J. 2015, *ApJ*, 803, 29